Room-temperature Modulation of Microwave Conductivity in Ferroelectric-gated Correlated Oxides

Shizai Chu[1], Yifei Hao[2], Shaopeng Feng[1], Xia Hong[2], Keji Lai*[1]

[1] Department of Physics, University of Texas at Austin, Austin TX 78712, USA

[2] Department of Physics and Astronomy & Nebraska Center for Materials and Nanoscience, University of Nebraska-Lincoln, Lincoln, NE 68588-0299, USA

* E-mails: kejilai@physics.utexas.edu

Abstract

We report the nonvolatile modulation of microwave conductivity in ferroelectric $PbZr_{0.2}Ti_{0.8}O_3$-gated ultrathin $LaNiO_3/La_{0.67}Sr_{0.33}MnO_3$ correlated oxide channel visualized by microwave impedance microscopy. Polarization switching is obtained by applying a tip bias above the coercive voltage of the ferroelectric layer. The microwave conductivity of the correlated channel underneath the up- and down-polarized domains has been quantified by finite-element analysis of the tip-sample admittance. At room temperature, a resistance on/off ratio above 100 between the two polarization states is sustained at frequencies up to 1 GHz, which starts to drop at higher frequencies. The frequence-dependence suggests that the conductance modulation originates from ferroelectric field effect control of carrier density. The modulation is nonvolatile, remaining stable after 6 months of domain writing. Our work is significant for potential applications of oxide-based ferroelectric-field-effect transistors in high-frequency nanoelectronics and spintronics.

At the heterointerface between a ferroelectric and a functional material, the polarization reversal of the former can lead to substantial modulation of various properties, such as electrical resistivity[1-3], magnetic order[4], magnetic anisotropy[5], spin texture[6], and superconductivity[7], in the latter. The effect is particularly important for strongly correlated oxides[8-10], where the carrier density is high and strong polarization fields are essential to induce appreciable changes in channel conduction. Such a combination of the nonvolatile nature of ferroelectric gating and sub-nanometer screening length in near-metallic correlated materials is highly desirable for low-power logic operations and memory functions[11-14]. To date, different combinations of ferroelectric thin films and correlated oxides have been studied for Mott ferroelectric-field-effect transistors (FeFETs)[9-17], and the field continues to attract strong interest from both scientific and engineering communities.

For electronic device applications of Mott FeFETs, the conductance modulation of channel materials has to persist up to the operation frequency, which is usually in the gigahertz (GHz) regime. While this is straightforward for traditional semiconductor-based transistors, it is not obvious if the requirement is met in complex oxides, where slow ionic conduction due to oxygen vacancies is not negligible[18]. In fact, conventional investigations of Mott FeFETs only evaluate the on/off conductance ratio at the DC limit. A powerful technique to assess the high frequency conductance of the correlated channel is microwave impedance microscopy (MIM).[19,20] In this work, we study the microwave conductivity of the epitaxial heterointerface between a ferroelectric layer and an ultrathin correlated oxide composite layer by MIM. Polarization reversal is achieved by applying a tip bias above the coercive voltage of the ferroelectric and confirmed by piezo-response force microscopy (PFM). The MIM contrast between the correlated oxide layer gated by the up- and down-polarized ferroelectric domains has been quantified by finite-element analysis

of the tip-sample admittance. At room temperature, the conductance on/off ratio between the two nonvolatile states is above 100 at frequencies up to 1 GHz, which drops at higher frequencies. The frequence-dependence suggests that the conductance modulation originates from ferroelectric field effect control of carrier density. The modulation is nonvolatile, remaining stable after 6 months of domain writing. Our results are important for further development of Mott FeFETs towards applications in high-frequency nanoelectronics and spintronics.

The epitaxial complex oxide heterostructure in this work consists of a 100 nm-thick ferroelectric $PbZr_{0.2}Ti_{0.8}O_3$ (PZT) thin film and a bilayer composite oxide of 1.2 nm or 3-unit-cell (u.c.) $LaNiO_3$ (LNO) and 0.8 nm or 2 u.c. $La_{0.67}Sr_{0.33}MnO_3$ (LSMO), as illustrated in Figure 1a. These layers were sequentially deposited on (001) $SrTiO_3$ (STO) substrates by off-axis radio frequency magnetron sputtering[15]. The LSMO layer was grown at 650 °C in 150 mTorr gas ($Ar:O_2$ = 2:1). The LNO and PZT layers were deposited at 500 °C with process gas of 60 mTorr ($Ar:O_2$ = 1:2) and 120mTorr ($Ar:O_2$ = 2:1), respectively. All layers are single crystalline along (001) orientations, as confirmed by X-ray diffraction (XRD) measurements (Fig. 1b). Atomic force microscopy (AFM) measurements reveal smooth sample surface with a typical root-mean-square roughness of 5 Å (Fig. 1b inset). In terms of functionality, the 3 u.c. LNO is the active conduction channel. While bulk LNO is a correlated metal, previous studies have shown that ultrathin LNO becomes a Mott insulator and exhibits a charge density-driven metal-insulator transition[15, 21-24]. The 2 u.c. LSMO, on the other hand, is well below the electric dead layer thickness and thus highly insulating[25]. It not only serves as a charge-transfer layer[26-28] that reduces the net carrier density in the LNO channel but also as an extended screening layer to mitigate the depolarization effect in the PZT thin film[9,15]. It has been shown previously that for the same channel thickness, the ferroelectric field effect in LNO/LSMO composite channels is orders of magnitude higher than

that in single-layer LNO channels.[15] All measurements to be discussed below were performed at room temperature, highlighting the technological relevance of our work.

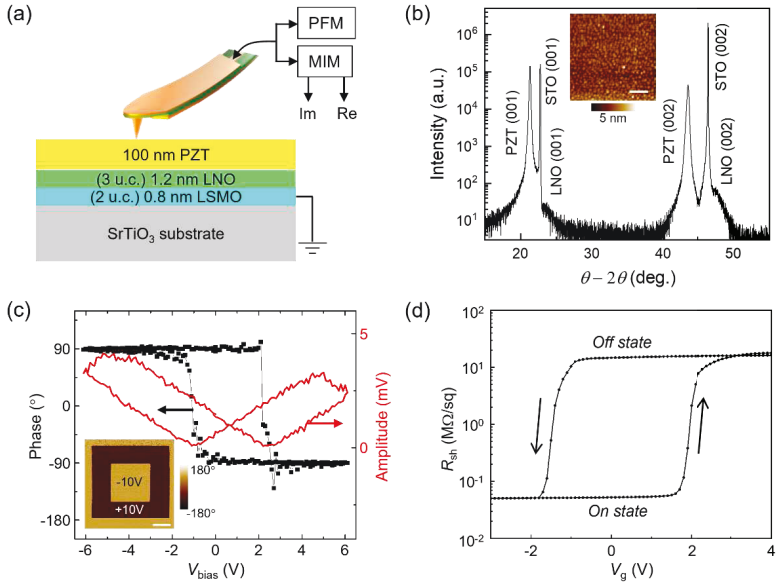

Fig. 1. **(a)** Schematics of the sample layer structure and the PFM/MIM experiments. **(b)** XRD θ–2θ scan taken on a PZT/LNO(3)/LSMO(2) heterostructure deposited on (001) STO. Inset: AFM topography image of the sample. The scale bar is 600 nm. **(c)** PFM phase the amplitude hysteresis loops of the PZT layer. Inset: PFM phase image of a pattern written by +10 V in the outer box and -10 V in the inner box. The scale bar is 4 μm. **(d)** Gate-dependent sheet resistance measured at room temperature showing an on/off ratio of 280 at the initial state.

Figure 1c shows the PFM switching hysteresis loop taken on a PZT/LNO(3)/LSMO(2) sample. The voltages to switch the up-polarized ($P\uparrow$) and down-polarized ($P\downarrow$) states are +2.3 V and –1.1 V, respectively, as seen from both the rectangular phase loop and butterfly-like amplitude loop. The difference in coercive fields indicates that $P\uparrow$ is the preferred state for as-grown films[15].

Next, we wrote 'box-in-box' patterns by applying ±10 V bias on the tip. As seen in the inset of Fig. 1c, the PFM phase image clearly shows the presence of $P\uparrow$ and $P\downarrow$ domains after the writing. The polarization state after writing with −10 V is the same as that of the unwritten film, which again suggests that the as-grown PZT is uniformly up-polarized. For DC transport measurement, we followed the method in Ref. [15] and patterned the sample into top-gated FET devices via photolithography. The in-plane (perpendicular to the *c*-axis) resistance is then measured by a Keithley 2400 SourceMeter and the result is converted to sheet resistance R_{sh} by the geometric factor. As shown in Fig. 1d, the gate-dependent R_{sh} exhibits a clear hysteresis loop, where the $P\uparrow$ ($P\downarrow$) polarization displays high (low) channel conduction, consistent with hole-type doping in LNO. The R_{sh} values for the on-state and off-state are 52.7 kΩ/sq and 14.8 MΩ/sq, respectively. A previous study[15] indicates that the relaxation of on- and off-state resistance usually stabilizes over several hours, with the on/off ratio reduced to about 55% of the initial value. We thus deduce a steady-state on/off ratio of about 150 at zero frequency for PZT/LNO(3)/LSMO(2).

The study of high-frequency conductance of the PZT-gated LNO channel was performed by MIM. As illustrated in Fig. 1a, the MIM is an AFM-based technique[29] that detects the tip-sample interaction at the range of frequency (*f*) from high-MHz to low-GHz. Signals from the two output channels, MIM-Re and MIM-Im, are proportional to the real and imaginary parts of the tip-sample admittance $Y_{t\text{-}s}$, respectively. Figures 2a and 2b show the MIM images of a box-in-box pattern taken at f = 104 MHz and 966 MHz, respectively. The contrast shows no sign of decay 6 months after the pattern writing, consistent with the nonvolatile nature of ferroelectric gating. Interestingly, while the MIM-Im signals in the $P\uparrow$ domain are higher than that in the $P\downarrow$ domain in both images, i.e., Δ_{Im} = Im($P\uparrow$) − Im($P\downarrow$) > 0, the MIM-Re contrast Δ_{Re} = Re($P\uparrow$) − Re($P\downarrow$) is opposite in sign for the two frequencies. In Figures 2c and 2d, we plot the histograms, i.e., number

of pixels versus signals, for f = 104 MHz and 966 MHz, respectively. The values and standard deviations of Δ_{Im} and Δ_{Re} can be readily extracted from Gaussian fits to the two peaks associated with signals in $P\uparrow$ and $P\downarrow$ domains.

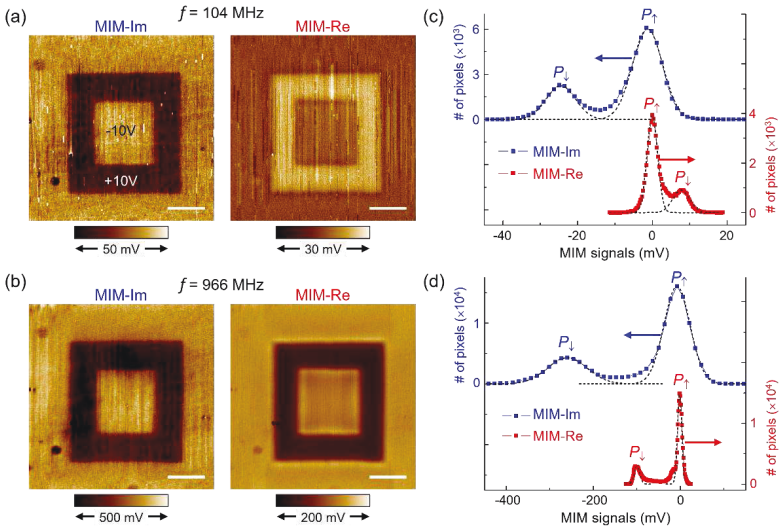

Fig. 2. (a) MIM-Im and MIM-Re images taken at 104 MHz and **(b)** 966 MHz. All scale bars are 5 μm. **(c)** Histogram of the MIM-Im and MIM-Re signals in (a). Peaks associated with the $P\uparrow$ and $P\downarrow$ states are marked in the plots. The dash lines represent Gaussian fits to individual peaks. Here Δ_{Im} = Im($P\uparrow$) – Im($P\downarrow$) = 24 ± 5 mV and Δ_{Re} = Re($P\uparrow$) – Re($P\downarrow$) = –7.5 ± 2.6 mV. **(d)** Histogram of the MIM-Im and MIM-Re signals in (b). Here Δ_{Im} = 260 ± 54 mV and Δ_{Re} = Re($P\uparrow$) – Re($P\downarrow$) = 96 ± 8 mV.

In order to quantify the MIM signals, we carried out finite-element analysis[30] using the AC/DC module of the commercial software COMSOL 6.0. As LSMO is below the dead-layer thickness, we assumed all conduction modulation originates from LNO. Taking the shape of tip apex from the scanning electron microscopy image (inset of Fig. 3) and the sample layer structure, we can simulate the real and imaginary parts of $Y_{t\text{-}s}$ as a function of the sheet conductance G_{sh} of

the LNO layer. The MIM response curves, which shift to lower (higher) G_{sh} at lower (higher) f, are flat when the sample is very conductive or very resistive. For intermediate G_{sh}, the MIM-Im signal increases monotonically and MIM-Re shows a peak, which is the 'sensitivity window' of this technique[19,20]. It should be noted that, due to background subtraction in MIM electronics[29], one cannot use the absolute signals in Fig. 2 to determine the local G_{sh}. The common practice is to find a region of the sample with known electrical properties as the reference[19,20]. Here, the on-state resistivity of the sample is around 10^{-3} to 10^{-2} Ohm·cm. For the frequency up to 10 GHz, this is well below the resistivity range of non-metallic conductors (well above 1 Ohm·cm) where the dielectric response is dominated by hopping, as depicted by Jonscher's Law of Universal Dielectric Response.[31] Indeed, the 3 u.c. LNO in this study is on the metallic side of the thickness-driven metal-insulator transition,[15] and the charge transfer at the LNO/LSMO interface does not change the metallicity of the active Mott channel at the PZT/LNO interface. As a result, it is reasonable to assume that the on-state AC conductance remains the same as the DC value up to GHz frequencies, i.e., $G_{sh}(\text{on}) = 1/R_{sh}(\text{on}) \sim 2 \times 10^{-5}$ S·sq (dash-dotted line in Figure 3). The off-state AC conductance $G_{sh}(\text{off})$ can be determined by comparing the ratio of Δ_{Re}/Δ_{Im}, which effectively cancels the scaling factor from $Y_{t\text{-}s}$ to MIM output, between experimental data and simulated curves. Qualitatively, the MIM contrast between $P\uparrow$ and $P\downarrow$ domains ($\Delta_{Re}/\Delta_{Im} \sim -0.3$ at 104 MHz and ~ +0.4 at 966 MHz) corresponds to $G_{sh}(\text{off}) \sim 2 \times 10^{-7}$ S·sq, as indicated by the shaded column in Figure 3. A large on/off ratio on the order of 100 thus persists up to the GHz regime in this sample, reaching about 120 at 1 GHz. Since ionic conduction due to oxygen vacancies cannot follow the fast AC electric fields at this frequency regime, we conclude that the dominant conduction mechanism in our device is electronic in nature. In this scenario, the strong polarization of PZT either accumulates or depletes the carrier density in LNO, resulting in a carrier-density-driven metal-insulator

transition. The ferroelectric polarization doping induced metal-insulator transition has previously been observed in 4 u.c. single layer LNO channels.[15] Since the modulation is electronic in nature, the zero-frequency resistance switching (Fig. 1d) can persist up to 1 GHz, till which electron/polaron hopping start to have notable contribution to the off-state conductance.[31]

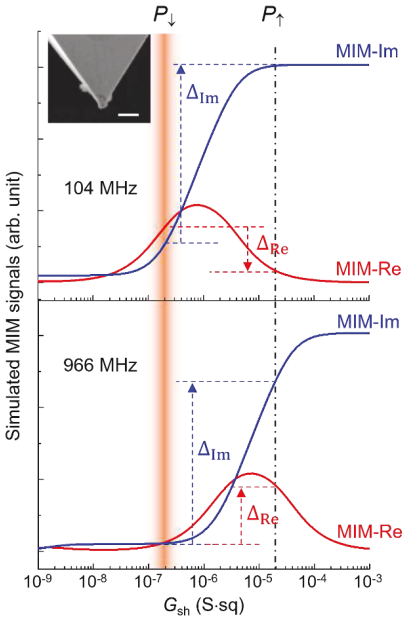

Fig. 3. Simulated MIM signals of the LNO layer at (top) 104 MHz and (bottom) 966 MHz. The on-state sheet conductance is assumed to be the same as the DC value of 2×10^{-5} S·sq. The shaded column indicates the estimated sheet conductance of the off-state. The MIM contrasts Δ_{Re} and Δ_{Im} are labeled in the plots. The inset shows a scanning electron microscopy image of the tip. The scale bar is 1 μm.

We extended the MIM study to cover a wide frequency range from 0.1 GHz to 6 GHz. In Fig. 4a, the false-color scale is adjusted such that all MIM-Im images appear to have the same contrast between $P\uparrow$ and $P\downarrow$ domains. In addition, the two MIM images at each frequency are plotted with the same color scale. It is clear that $\Delta_{Re} = \mathrm{Re}(P\uparrow) - \mathrm{Re}(P\downarrow)$ is negative at ~ 100 MHz,

approaches zero at ~ 300 MHz, turns positive at ~ 1 GHz and continues to increase at higher frequencies. Using the same analysis as above, we estimated the *f*-dependent G_{sh}(off) and on/off ratio. As summarized in Fig. 4b, the on/off ratio exhibits weak frequency-dependence over a wide range of operating frequency up to ~ 1 GHz and starts to drop at higher frequencies. For correlated oxide materials, ultrafast spectroscopy studies[32] indicate that the characteristic time scale for structure-related transition is on the order of 100 ps. It is possible that the lattice degree of freedom is responsible for the increase of G_{sh}(off) and decrease of on/off ratio at frequencies above 1 GHz. Note that the off-state resistivity is on the order of 1 Ohm·cm, where the universal dielectric response[31] starts to apply. In that case, the observed frequency-dependent conduction modulation provides another example of the empirical Jonscher-law behavior,[31] with the electron or polaron hopping being the underlying mechanism. Further experimental and theoretical works are needed to explain the *f*-dependent on/off ratio observed in this study.

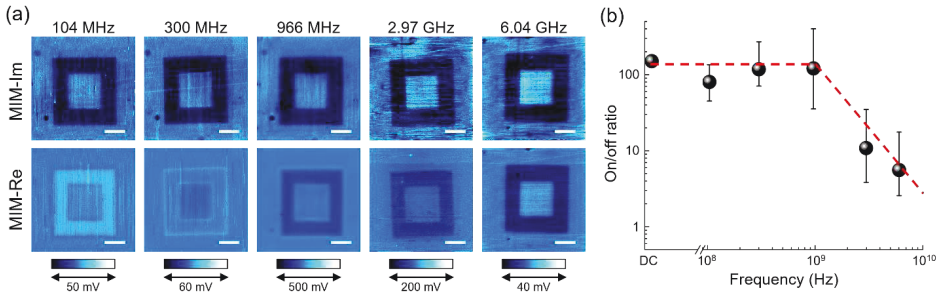

Fig. 4. (a) From left to right: MIM images taken at 104 MHz, 300 MHz, 966 MHz, 2.97 GHz, ad 6.04 GHz. The color scales are adjusted such that all MIM-Im images display the same contrast between the two domains and each pair of the MIM-Im/Re images at the same frequency share the same color scale. All scale bars are 5 μm. **(b)** Frequency-dependent on/off ratio extracted from the MIM data. The red dashed lines are guides to the eyes.

In summary, we report the high-frequency conductivity imaging of ultrathin correlated oxides with ferroelectric gating by microwave impedance microscopy. Polarization reversal is achieved by applying a tip bias beyond the coercive voltage. The MIM contrast between the up- and down-polarized domains can be quantified by finite-element analysis of the tip-sample admittance. The observed room-temperature resistance ratio between the two nonvolatile states is on the order of 100 from DC to 1 GHz and drops at higher frequencies. The result confirms that the large on/off ratio originates from the field-effect modulation of charge density rather than ionic conduction. Our work is significant for potential applications of Mott FeFETs in high-frequency nanoelectronics and spintronics.

This work is supported by the NSF Division of Materials Research Grant DMR-2118806 and the Welch Foundation Grant F-1814. The work by XH and YH is supported by NSF DMR-2118828 and OIA-2044049.

AUTHOR DECLARATIONS

Conflict of Interest

K.L. holds a patent on the MIM technology, which is licensed to PrimeNano Inc. as a commercial instrument. The terms of this arrangement have been reviewed and approved by the University of Texas at Austin in accordance with its policy on objectivity in research.

DATA AVAILABILITY

The data that support the findings of this study are available from the corresponding author upon reasonable request.

References

[1] C. H. Ahn, A. Bhattacharya, M. Di Ventra, et al. Electrostatic modification of novel materials. Rev. Mod. Phys. **78**, 1185 (2006).

[2] C. Ko , Y. Lee, Y. Chen, et al. Ferroelectrically gated atomically thin transition-metal dichalcogenides as nonvolatile memory. Adv. Mater. **28**, 2923-2930 (2016).

[3] A. Lipatov, A. Fursina, T. H. Vo, et al. Polarization‐Dependent Electronic Transport in Graphene/Pb(Zr, Ti)O_3 Ferroelectric Field-Effect Transistors. Adv. Elec. Mater. **3**, 1700020 (2017).

[4] X. Hong, A. Posadas, A. Lin, et al. Ferroelectric-field induced tuning of magnetism in the colossal magnetoresistive oxide $La_{1-x}Sr_xMnO_3$. Phys. Rev. B **68**, 134415 (2003).

[5] A. Rajapitamahuni, L. L. Tao, Y. Hao, et al. Ferroelectric polarization control of magnetic anisotropy in $PbZr_{0.2}Ti_{0.8}O_3/La_{0.8}Sr_{0.2}MnO_3$ heterostructures. Phys. Rev. Mater. **3**, 021401 (2019).

[6] L. Wang., Q. Feng., Y. Kim, et al. Ferroelectrically tunable magnetic skyrmions in ultrathin oxide heterostructures. Nat. Mater. **17**, 1087 (2018).

[7] C. H. Ahn, S. Gariglio, P. Paruch, et al. Electrostatic modulation of superconductivity in ultrathin $GdBa_2Cu_3O_{7-x}$ films. Science **284**, 1152 (1999).

[8] C. H. Ahn, J. M. Triscone, & J. Mannhart. Electric field effect in correlated oxide systems. Nature **424**, 1015 (2003).

[9] X. Chen, X. Zhang, M. A. Koten, et al. Interfacial charge engineering in ferroelectric controlled Mott transistors. Adv. Mater. **29**, 1701385 (2017).

[10] H. Yamada, M. Marinova, P. Altuntas, et al. Ferroelectric control of a Mott insulator. Sci. Rep. **3**, 2834 (2013).

[11] X. Hong, Emerging ferroelectric transistors with nanoscale channel materials: the possibilities, the limitations. J. Phys. Condens. Matter **28**, 103003 (2016).

[12] Y. Watanabe, Epitaxial all-perovskite ferroelectric field-effect transistor with a memory retention. Appl. Phys. Lett. **66**, 1770 (1995).

[13] J. Hoffman, X. Hong, & C. H. Ahn, Device performance of ferroelectric/correlated oxide heterostructures for non-volatile memory applications. Nanotechnology **22**, 254014 (2011).

[14] C. A. F. Vaz, Y. J. Shin, M. Bibes, et al. Epitaxial ferroelectric interfacial devices. Appl. Phys. Rev. **8**, 041308 (2021).

[15] Y. Hao, X. Chen, L. Zhang, et al. Record high room temperature resistance switching in ferroelectric-gated Mott transistors unlocked by interfacial charge engineering. Nat. Commun. **14**, 8247 (2023).

[16] A. Malashevich, M. S. J. Marshall, C. Visani, et al. Controlling mobility in perovskite oxides by ferroelectric modulation of atomic-scale interface structure. Nano Lett. **18**, 573-578 (2018).

[17] J. Y. Kim, M. Choi, H. W. Jang, et al. Ferroelectric field effect transistors: Progress and perspective. APL Mater. **9**, 021102 (2021).

[18] J. A. Kilner, & R. J. Brook, A study of oxygen ion conductivity in doped non-stoichiometric oxides. Solid State Ionics **6**, 237 (1982).

[19] K. Lai, W. Kundhikanjana, Z. X. Shen, Nanoscale microwave microscopy using shielded cantilever probes. Appl. Nanosci. **1**, 13 (2011).

[20] Z. Chu, L. Zheng, K. Lai, Microwave Microscopy and Its Applications. Annu. Rev. Mater. Res. **50**, 105 (2020).

[21] R. Scherwitzl, S. Gariglio, M. Gabay, et al. Metal-insulator transition in ultrathin $LaNiO_3$ films. Phys. Rev. Lett. **106**, 246403 (2011).

[22] J. Fowlie, M. Gibert, G. Tieri, et al. Conductivity and local structure of $LaNiO_3$ thin films. Adv. Mater. **29**, 1605197 (2017).

[23] M. Golalikhani, Q. Lei, R.U. Chandrasena, et al. Nature of the metal-insulator transition in few unit-cell-thick $LaNiO_3$ films. Nat. Commun. **9**, 2206 (2018).

[24] S. Catalano, M Gibert, J Fowlie, et al. Rare-earth nickelates $RNiO_3$: thin films and heterostructures. Rep. Prog. Phys. **81**, 046501 (2018).

[25] R. P. Borges, W. Guichard, J. G. Lunney, et al. Magnetic and electric "dead" layers in $(La_{0.7}Sr_{0.3})MnO_3$ thin films. J. Appl. Phys. **89**, 3868-3873 (2001).

[26] J. Hoffman, I. C. Tung, B. B. Nelson-Cheeseman, et al. Charge transfer and interfacial magnetism in $(LaNiO_3)_n/(LaMnO_3)_2$ superlattices. Phys. Rev. B **88**, 144411 (2013).

[27] M. Kitamura, K. Horiba, M. Kobayashi, et al. Spatial distribution of transferred charges across the heterointerface between perovskite transition metal oxides $LaNiO_3$ and $LaMnO_3$. Appl. Phys. Lett. **108**, 111603 (2016).

[28] H. Chen, & A. Millis, Charge transfer driven emergent phenomena in oxide heterostructures. J. Phys. Condens. Matter **29**, 243001 (2017).

[29] K. Lai, M. B. Ji, N. Leindecker, et al. Atomic-force-microscope-compatible near-field scanning microwave microscope with separated excitation and sensing probes. Rev. Sci. Instrum. **78**, 063702 (2007).

[30] K. Lai, W. Kundhikanjana, M. Kelly, et al. Modeling and characterization of a cantilever-based near-field scanning microwave impedance microscope. Rev. Sci. Instrum. **79**, 063703 (2008).

[31] A. K. Jonscher, The 'universal' dielectric response. Nature **267**, 673-679 (1977).

[32] Z. Yang, C. Ko, and S. Ramanathan, et al. Oxide electronics utilizing ultrafast metal-insulator transitions. Annu. Rev. Mater. Res. **41**, 337-367 (2011).